Electronic Supplementary Information

Modular 3D printed flow system for efficient one-step synthesis of phenyl-functionalised silica-coated superparamagnetic iron oxide nanoparticles

Andrea du Preez[1], André M. Strydom[2], Derek T. Ndinteh[1], Elize Smit[1]

[1]*Center for Natural Product Research, Department of Chemical Sciences, University of Johannesburg, Johannesburg, South Africa*

[2]*Highly Correlated Matter Research Group, Department of Physics, University of Johannesburg, Auckland Park, South Africa*

Corresponding author:

Elize Smit: esmit@uj.ac.za

Contents

List of Figures

Fluidic device channel geometry

Initially, three different fluidic devices with different channel geometries were used for the synthesis of bare IONPs. Figure S1 illustrates the rudimentary channel geometries that were incorporated into three-dimensional fluidic reactor designs. The three different reactor channel geometry types can be described as follows: A classic T-reactor where channels meet head-on, a Y-reactor, and an alternative T-reactor where the channels meet perpendicularly. Furthermore, the channels of these devices were labelled in order to describe the size and shape of each device.

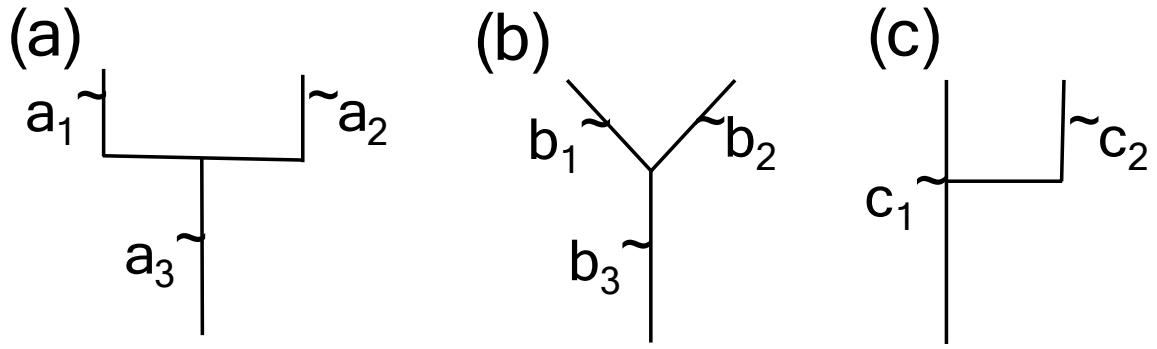

Figure S1: Illustrations of three different fluidic reactor channel geometries. (a) A classic T-reactor with head-on channels labelled a_1-a_3. (b) A Y-reactor with channels labelled b_1 – b_3. (c) A perpendicular channel T-reactor with channels labelled c_1 and c_2.

All channels were initially modelled to be cylindrical with a 1 mm diameter. Since all channels are of the same size (1 mm diameter), chaotic mixing occurred in all devices regardless of channel geometry, as shown in Figure S2. To mitigate clogging by aggregation, the reactors were redesigned with wider reaction zones (2 mm). Detailed images of the T-reactor, Y-reactor and perpendicular channel T-reactor are provided in Figures S3, S4 and S5, respectively.

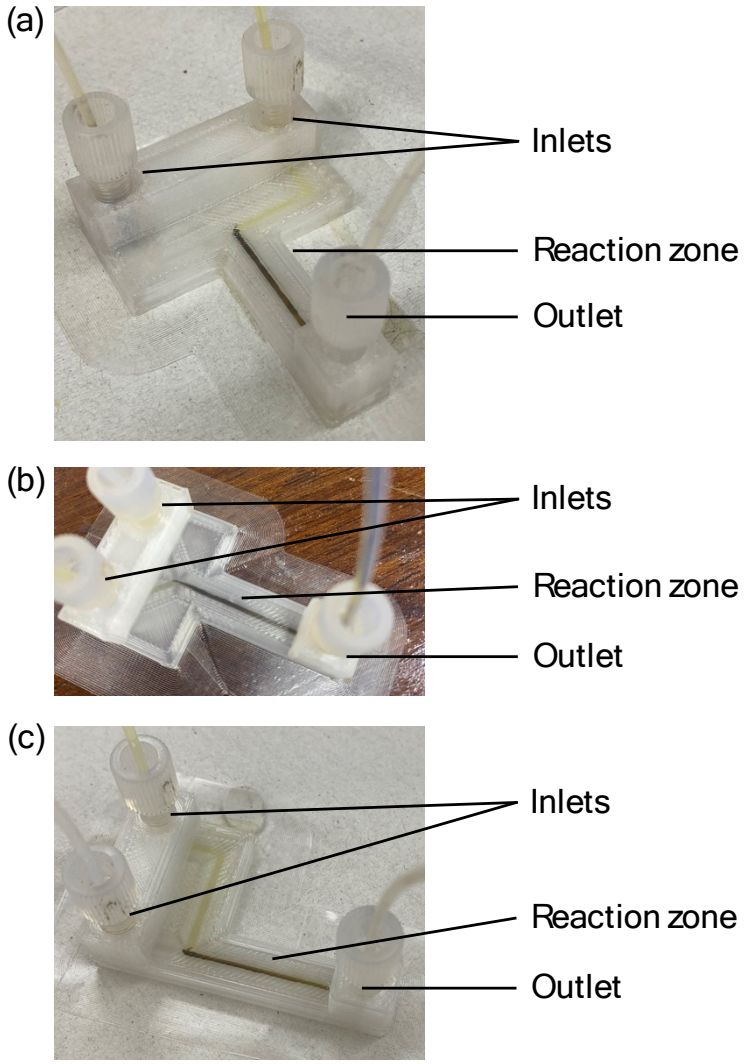

Figure S2: 3D-printed PP fluidic devices (1 mm channel diameters) used for synthesising bare IONPs during preliminary experiments. Since all devices had channels of 1 mm diameter, chaotic mixing occurred. (A) Head-on T-reactor. (B) Perpendicular channel T-reactor. (C) Y-reactor.

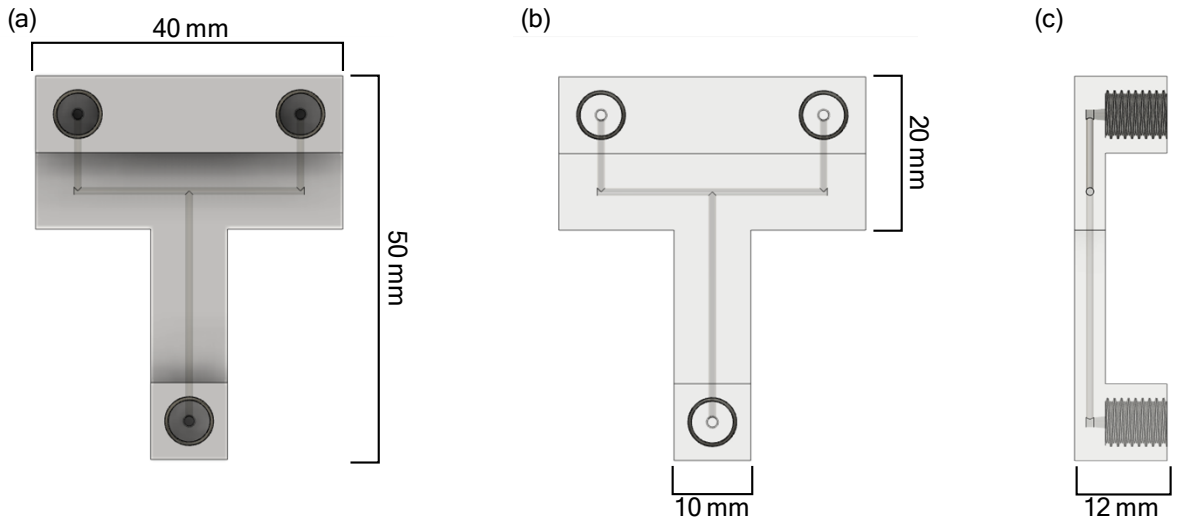

Figure S3: Diagram of the T-reactor design showing (a) top, (b) bottom and (c) side views. This reactor proved to be unsuitable during preliminary experiments since chaotic mixing occurred, resulting in nanoparticle agglomeration and device fouling. All channels were cylindrical and modelled to be 1 mm in diameter.

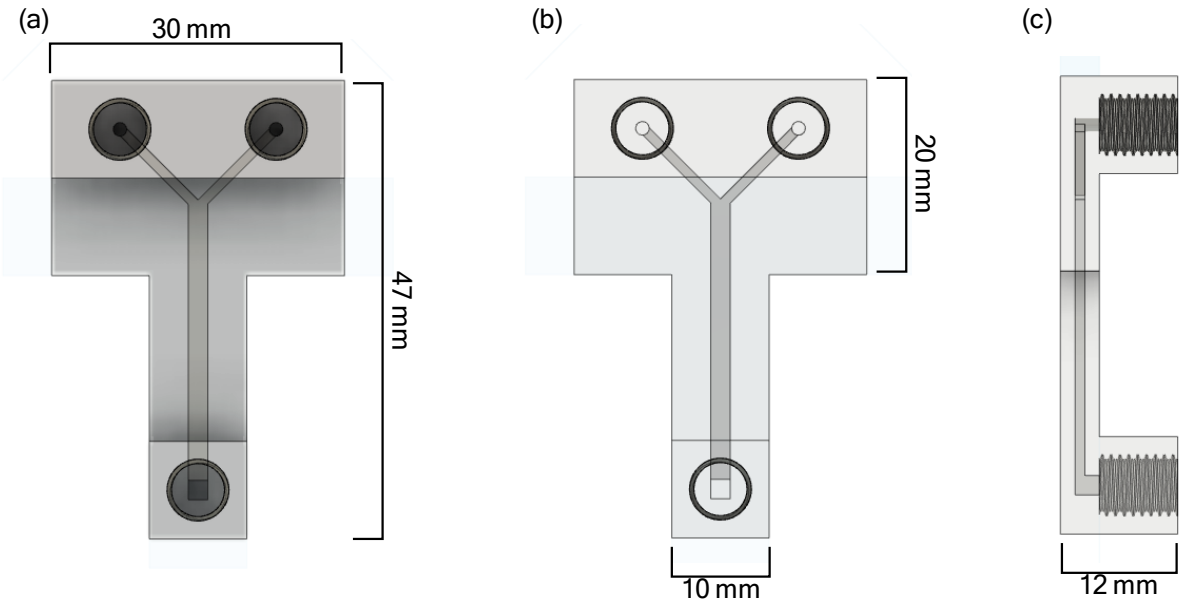

(d)

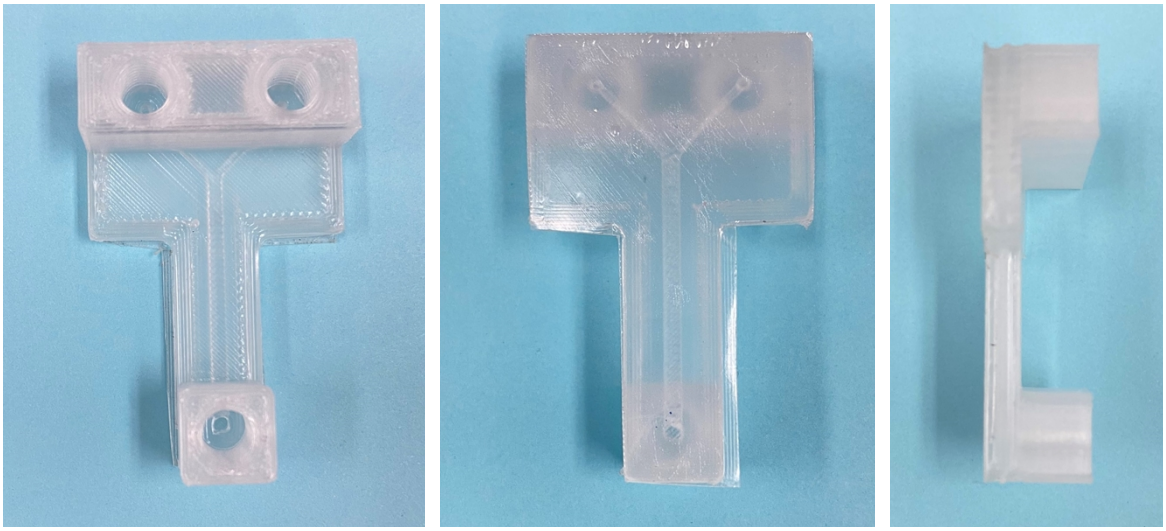

Figure S4: Diagram of the Y-reactor design showing (a) top, (b) bottom and (c) side views, together with corresponding photos of the 3D printed reactor (d).

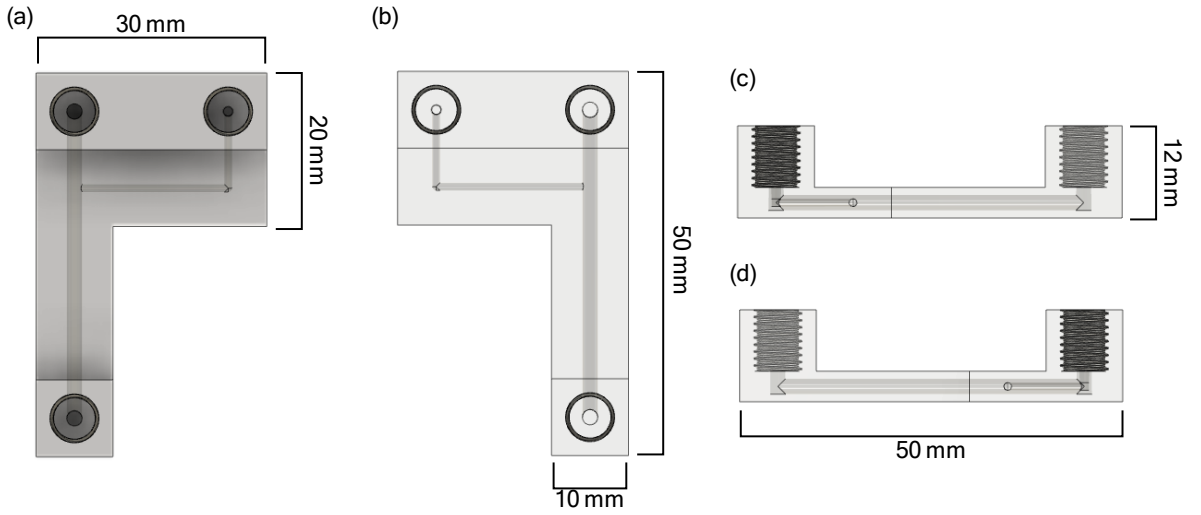

(e)

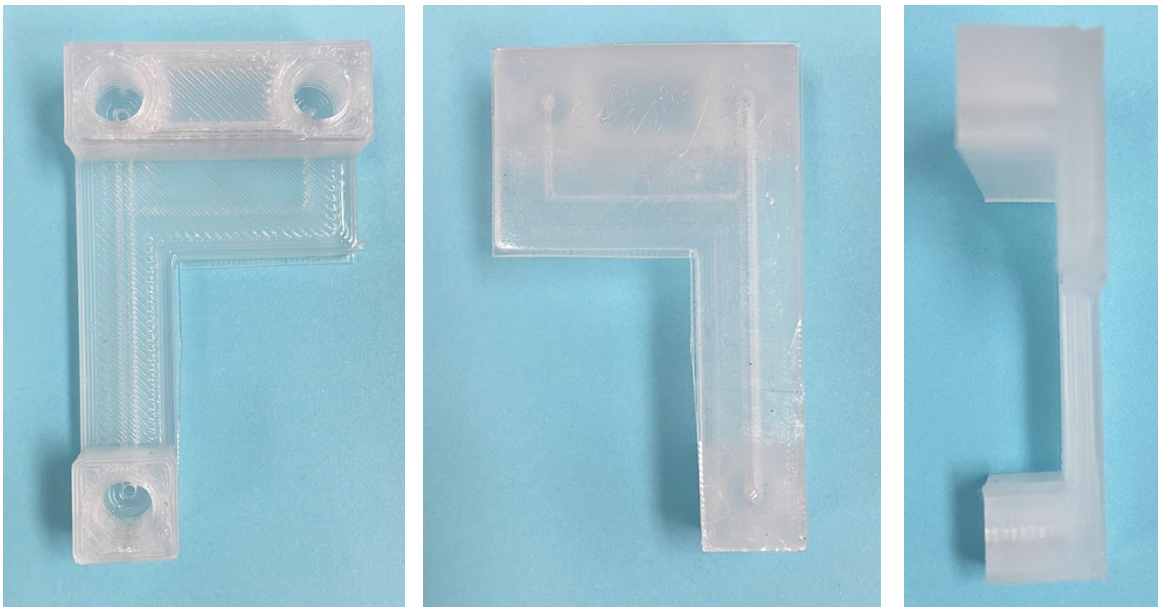

Figure S5: Diagram of the perpendicular channel T-reactor design showing (a) top, (b) bottom, (c) left and (d) right side views, together with photos of the 3D printed reactor (e).

STL files

The STL files provided are as follows:

T-reactor.stl	The T-reactor with 1 mm channel diameters (Figure S3).
Y-reactor.stl	The Y-reactor (Figure S4).
Perpendicular channel reactor.stl	The perpendicular channel T-reactor (Figure S5).

Fabrication of flow system components

The 3D printing conditions are provided in the full text. Default printing speeds were used and are summarised in Table S1. The following line was added to the G-code script (Printer settings > Custom G-code) to obtain an extruder flow of 105 %:

```
M221 S{if layer_height<0.075}100{else}105(endif)
```

Table S1: Printing speed parameters

Printing speed parameters	**Speed (mm/s)**
Perimeters	60
Infill	50
Solid Infill	20
First layer speed	30
Maximum print speed	80
Maximum feedrate (X)	200
Maximum feedrate (Y)	200
Maximum feedrate (Z)	12
Maximum feedrate (E)	120

Flow system setup and operation

A PerkinElmer Clarus 580 gas chromatograph with a flame ionization detector (GC-FID) was used to investigate if any organic impurities were present in the flow system before the synthesis of IONPs. Isopropanol was used and analyzed before and after being passed through the flow system. The GC-FID was fitted with a RxiGuard column (10 m, 0.25 mm I.D.) and a Rxi-5HT column (30 m, 0.24 mm I.D.). A 1.00 µL sample was injected. Helium was used as the carrier gas with a 1.00 mL/min flow rate and a split ratio of 20:1. The GC oven temperature reached 60 °C initially with a 1 min hold and ramped up to 300 °C at 40 °C/min with a 10 min hold. In Figure S6, the overlayed chromatograms of isopropanol before (black) and after (red) being passed through the flow system are shown. No significant differences between the two chromatograms are visible except for differences in peak intensities. GC is a very sensitive technique (since it can readily detect compounds at 1 ppm levels) and trace impurities were detected before and after passing through the flow system. Since these impurities were present beforehand, they cannot be attributed to the flow system. Thus, no organic impurities were leached from the 3D-printed devices, and the PP was compatible with the solvents used.

Figure S6: The overlayed GC-FID chromatograms of isopropanol before (black) and after (red) being flowed through the flow system.

Variations in potential combinations of the flow reactors, to illustrate modularity and customisability are shown in Figure S7. Some tested and conceptualised flow systems are illustrated. The configuration shown in Figure S7(a) was used to synthesise bare IONPs. The configuration in Figure S7(b) was used synthesise the IONPs in the first reactor (R_1), followed by subsequent coating and functionalisation in the second reactor (R_2). Figure S7(c) shows a conceptualised system where the coating and functionalisation occur in separate reactors (R_1 and R_2). This configuration may be useful in instances where the coating and functionalisation must be done separately (but still sequentially). Perceived scenarios include when different reagents are required for functionalisation (e.g. if it is not based on triethylsiloxane derivatives) or if functionalisation cannot be performed simultanesouly with the silica coating step (e.g. if undesired byproducts are formed). Due to the changes in channel diameters, a configuration where the Y-reactor is placed after the perpendicular channel reactor was not considered here. Going to a narrower channel may result in undesired backpressure or clogging by agglomeration. Enlarging one of the inlet channels to avoid this, would also be undesirable, since the reaction zone geometry and ability to achieve laminar flow will be influenced by the junction of the inlet channels.

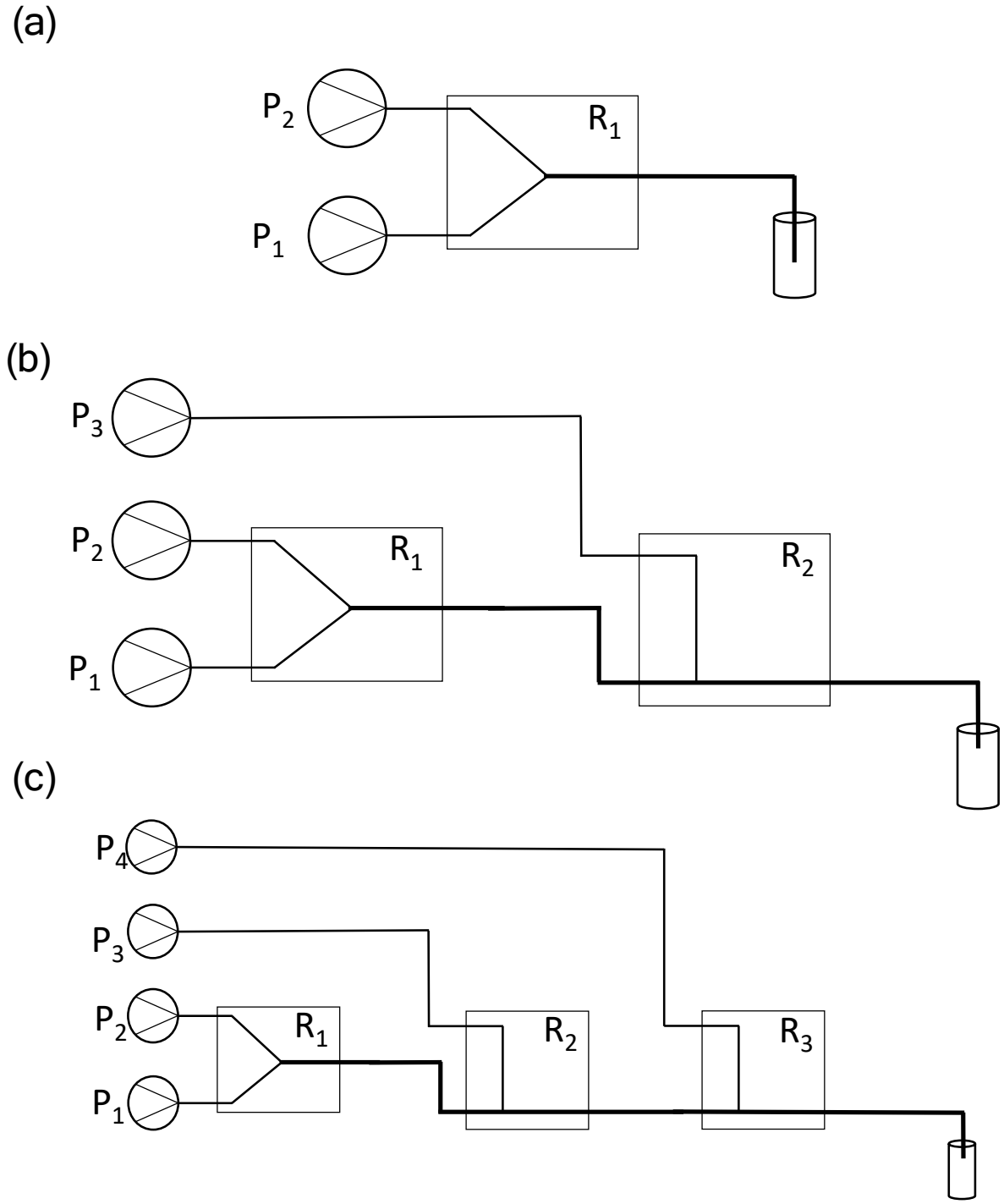

Figure S7: Diagrams indicating various flow systems that can be set up with the developed fluidic devices. Up to four pumps (P_1 – P_4) can be used to deliver reagents to up to three reactors (R_1 – R_3).

Material characterisation

FTIR

FTIR spectroscopy was used to track and subsequently optimise the synthetic steps for the flow synthesis of the modified magnetic nanoparticles. In Figure S8, the absorption bands at around 1615 cm^{-1} and 3230 – 3316 cm^{-1} were assigned to the H-O-H stretching modes and bending vibrations of free and absorbed water, respectively.[1,2] Similarly, the peak at around 1418 cm^{-1} corresponds to the C-O stretching vibration of atmospheric CO_2.[3] The BIONPs had a characteristic absorption band at 548 cm^{-1}, corresponding to the stretching vibration of Fe-O.[4] The SIONPs had an absorption band at around 1058 cm^{-1}, which can be assigned to the stretching vibrations of Si-O-Si in silica.[1] For all modified IONPs, the Fe-O vibration mode persisted from approximately 558 cm^{-1} to 567 cm^{-1} but with less intensity. This observation could explain the presence of a SiO_2 layer in all modified IONPs.[5] Additional peaks at 696 cm^{-1} and 733 cm^{-1} started to appear at higher TEPS concentrations (33.5-50.0% TEPS), which falls within the range (690-900 cm^{-1}) where out-of-plane (oop) bending for =C-H appears.[6] The stretching vibrations of Si-O-Si in silica were also observed between 1030 cm^{-1} and 1062 cm^{-1} for the PSIONPs (11.0-50.0% TEPS). However, an additional peak appeared at around 1132 cm^{-1} at higher TEPS concentrations (33.5-50.0% TEPS), which was assigned to be due to the Si-O-C bending vibration.[6] Furthermore, the characteristic =C-H (sp^2) stretching mode for aromatic rings[6–8] was only observed at higher TEPS concentrations (33.5-50.0% TEPS) at approximately 3053 cm^{-1}. The intensity of the broad peak at around 1615 cm^{-1} started to decrease and ultimately disappeared with increasing TEPS concentrations. Furthermore, this absorption band was eventually replaced with a much weaker signal at around 1595 cm^{-1}, which was also present in the FT-IR spectrum of TEPS (Figure S9) and could be due to the C=C stretching band of aromatic rings.[9] Lastly, the C-O absorption band at around 1418 cm^{-1} due to atmospheric CO_2 appears to be overlapped with a new absorption band at 1430 cm^{-1} when 33.5-50.0% TEPS concentrations were used. This signal was also assigned to be due to the C=C aromatic ring stretching vibrations.[7,8] Lastly, the FT-IR spectra for 5.0% TEPS and 44.5% TEPS were omitted for clarity since the obtained spectra were similar to those of 11.0% and 33.5% TEPS, respectively. Even though the concentration is relatively low and a bulk analytical technique was used, the diagnostic C=C peaks were observed, and become more prominent as more TEPS is incorporated into the system.

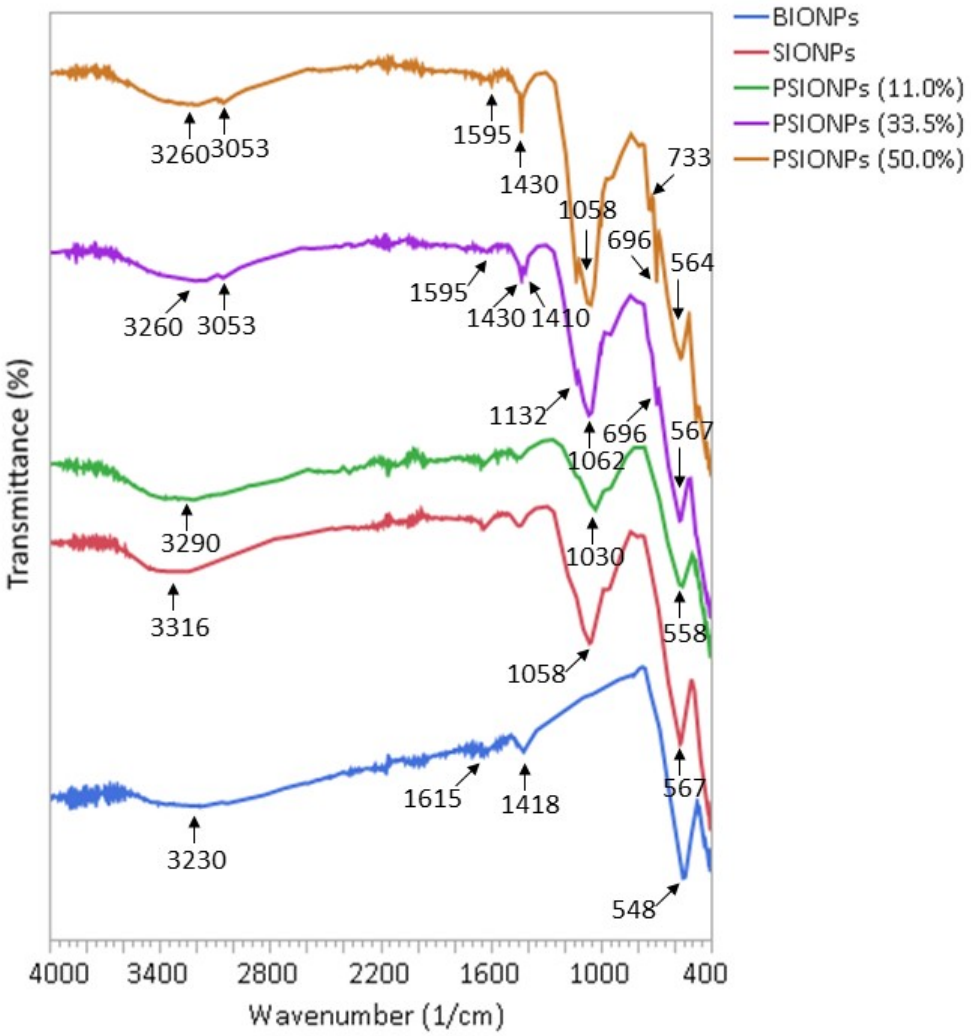

Figure S8: FTIR spectra of BIONPs, SIONPs, and PSIONPs using different percentages of TEPS in TEOS solutions (11.0%, 33.5%, and 50.0%).

The FTIR spectrum of TEPS is given in Figure S9. The C=C stretching bands for aromatic rings usually occur in pairs at 1600 cm^{-1} around 1475 cm^{-1} and can be observed at 1595 cm^{-1} and 1482 cm^{-1} in Figure S9, respectively. The =C-H (sp^2) absorption band appeared characteristically at values >3000 cm^{-1}, and the =C-H (oop) bending occurred in a range from 690 cm^{-1} to 900 cm^{-1}. Furthermore, the Si-O-C bending vibration was identified at around 1126 cm^{-1}, and the Si-O-Ph occurred near 1000 cm^{-1}. Moreover, the wavenumbers highlighted in red (Figure S9) were the peaks observed in the FTIR spectra of the modified IONPs (Figure S8) at higher TEPS concentrations (33.5-50.0% TEPS).

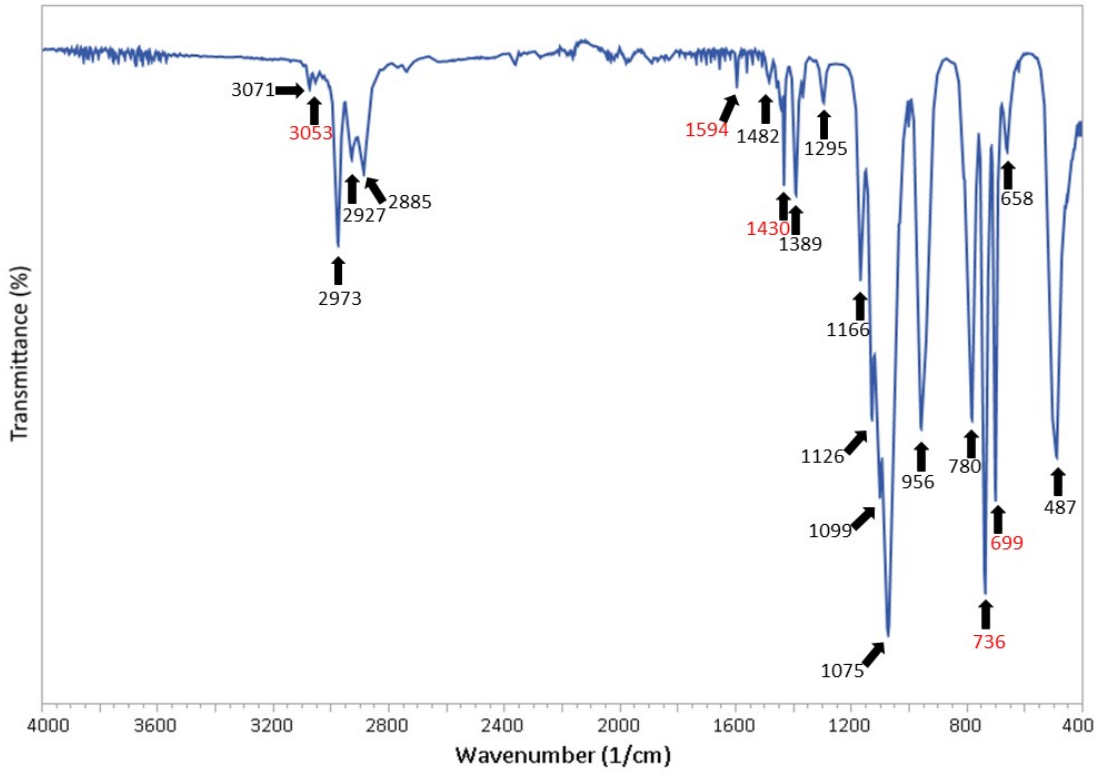

Figure S9: FTIR spectrum of TEPS with absorption bands labelled in red that occurred at higher TEPS concentrations (33.5-50.0% TEPS) for synthesising PSIONPs.

TEM

EDS analysis was used to confirm the presence of the expected elements in the synthesised IONPs. As expected, the BIONPs consisted of Fe and O (Figure S10(A)). The other elements present in the spectrum (C and Cu) originate from the carbon-coated copper grids used to analyse the samples. In Figure S10(B), the presence of Si was confirmed for the SIONPs together with Fe and O. Figure S10(C) shows the spectrum for the PSIONPs using a 50.0% TEPS in TEOS solution. These IONPs also consist of Fe, O, and Si. However, since the grids used for analysis were coated with carbon, the presence of C in the spectrum cannot be used to confirm the presence of an aromatic ring after functionalisation with TEPS. Lastly, the EDS spectra obtained for all other synthesised PSIONPs, using concentrations <50% TEPS, appeared similar.

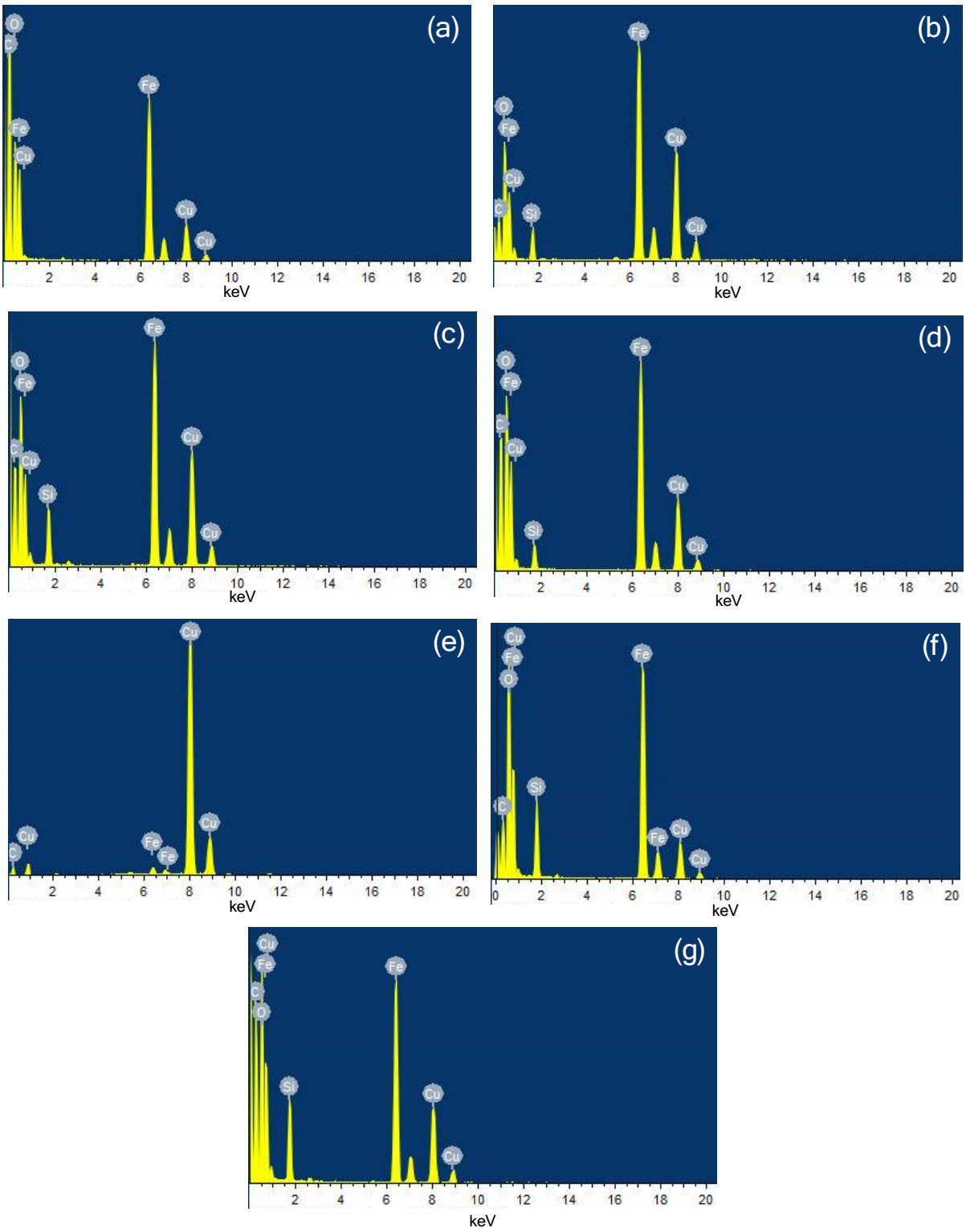

Figure S10: EDS spectra of (a) BIONPs, (b) SIONPs, and PSIONPs using a (c) 50.0%, (d) 5.0%, (e) 11.0%, (f) 33.5% and (g) 44.5% TEPS in TEOS solution.

Zeta potential

To estimate the isoelectric point (IEP) of the synthesised IONPs, the surface charge of these IONPs had to be measured at different pH values. The zeta potential as a function of pH for the synthesised IONPs is shown in Figure S11. The IEP, or in other words, the point of zero charge for the BIONPs was found to be at a pH of approximately 7.05 (Figure S11). Generally, IEP values for magnetite can range between 6.5-7.0.[10] Additionally, Schaminger et al.[11] reported an IEP at a pH of 7.0 for magnetite. The IEP decreased to approximately 3.7 after coating the BIONPs with silica. This significant decrease is due to the presence of terminal silanol groups after coating with silica.[12] The obtained IEP and zeta potential curve of SIONPs are comparable to that reported by Pinheiro et al.[13] It can be suggested that functionalisation did not occur when using a TEPS in TEOS percentage of 5.0%, since the IEP and zeta potential curve are similar to that obtained for the SIONPs and was consistent with the FTIR spectrum which showed no sign of the presence of phenyl groups on the nanoparticle surface. The IEP values varied from approximately 4.6 to 5.5 when functionalising the IONPs surface with phenyl groups with solutions containing 11.0-50.0% TEPS in TEOS. From literature[7], the zeta potential values for PSIONPs were negative from a pH of approximately 3.5; this was due to the fact that phenyl groups decrease the effects of hydroxyl groups on the nanoparticle surface. However, in the PSIONPs synthesised here, slightly higher IEP values were obtained since a mixture of phenyl and hydroxyl groups was present on the surface. Lastly, in all cases, the zeta potential decreased with an increase in pH.

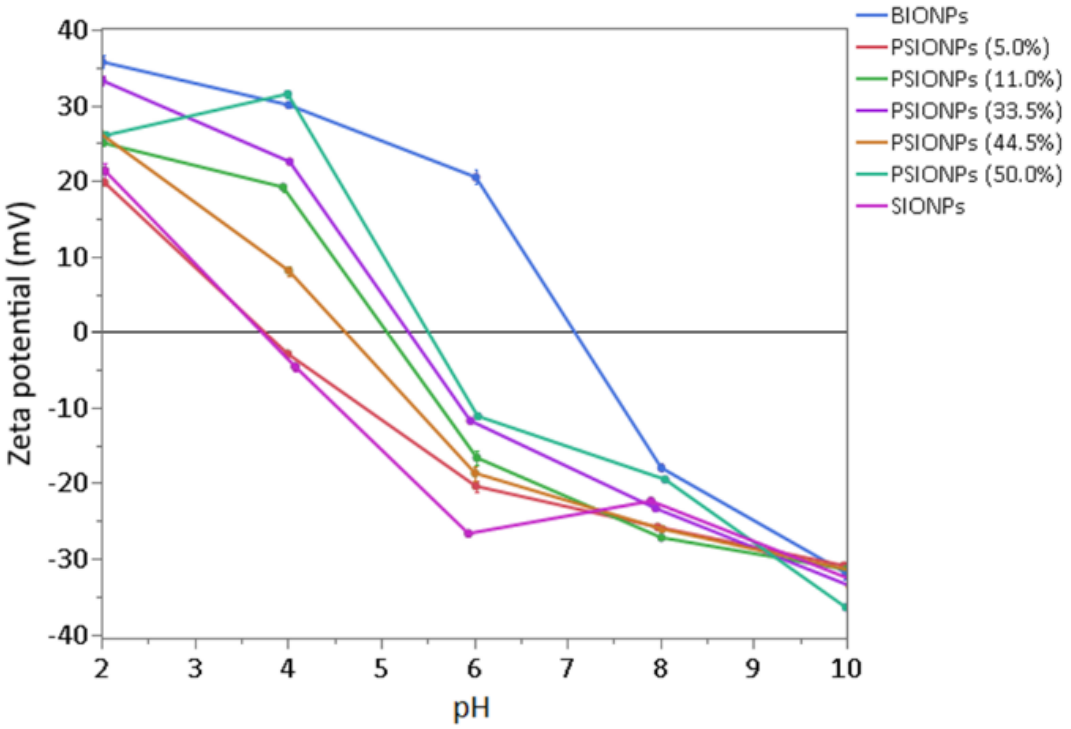

Figure S11: Zeta potential as a function of pH for BIONPs, SIONPs, and PSIONPs using 5.0-50.0% TEPS in TEOS solutions.

XRD

The XRD patterns of the synthesised IONPs in flow are shown in Figure S12. The XRD pattern for the BIONPs (Figure S12) showed characteristic diffraction peaks at 2θ values of 30.07°, 35.41°, 43.04°, 53.39°, 56.91°, and 62.50° which correspond to the crystal planes (220), (311), (400), (422), (511), and (440) respectively. The obtained XRD pattern is also comparable to reported patterns for BIONPs.[12,14] Moreover, the XRD pattern also agrees with the Inorganic Crystal Structure Database (ICSD, 01-076-1849) for magnetite with a face-centred cubic structure. The broad hump with 2θ values ranging from approximately 16° to 26° is indicative of the presence of the amorphous silica shell[6,15,16] and was present for all coated and functionalised IONPs (Figure S12). Since the peak positions identified for BIONPs (2θ values from 30.07° to 62.50°) are similar for the coated and functionalised IONPs (Figure S12), it can be deduced that the crystalline phase of the IONPs was not significantly altered during the coating and functionalisation processes.[1,12,17] However, the intensity for these peaks were decreased (Figure S12), which can be attributed to the silica coating.[18] From the XRD pattern of the PSIONPs (50.0%, Figure S12), the intensity of the broad hump (2θ values from 16° to 26°) decreased significantly. This observation is due to the decrease in the amount of TEOS in

the solution (50.0% v/v). This observation is indicative of a decrease in the thickness of the silica shell.[15] The XRD patterns for the PSIONPs (Figure S12) are comparable to literature.[6,19] Lastly, the obtained XRD patterns for the PSIONPs (11.0% and 44.5%) were omitted for clarity since they were similar to those in Figure S12.

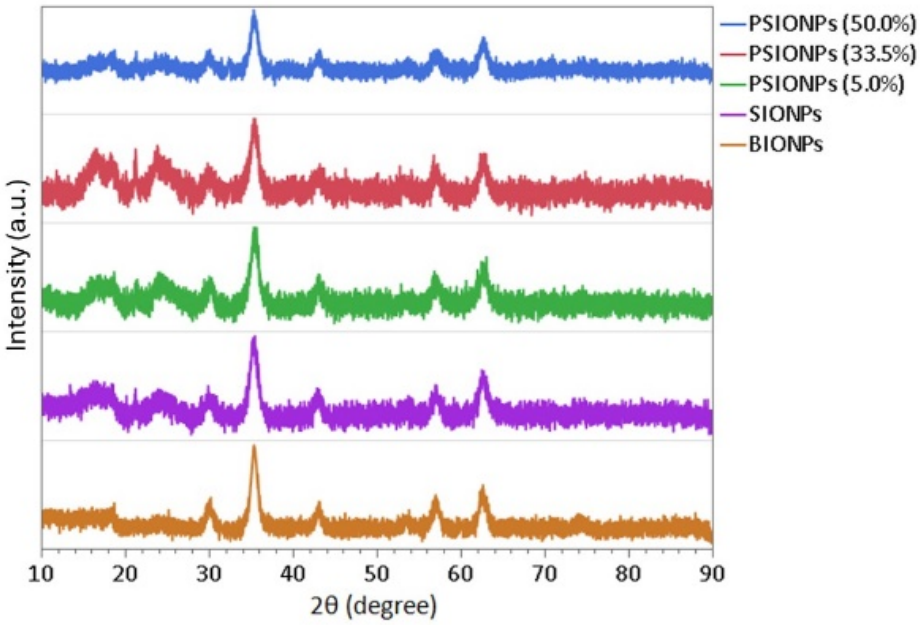

Figure S12: XRD pattern of BIONPs, SIONPs, and PSIONPs using 5.0%, 33.5% and 50.0% TEPS in TEOS solutions.

The crystalline size diameters (d) of the synthesised IONPs in flow were determined using the Scherer equation: $d = k\lambda/\beta\cos\theta$, where k is the grain shape factor ($k = 0.94$), λ is the incident wavelength ($\lambda = 1.54$ Å), β is the full width at half-maximum (FWHM) in radians, and θ the Bragg diffraction angle.[20] All calculated crystalline size diameters (Table 3) are comparable with the results obtained from TEM.

TGA

Thermogravimetric analysis (TGA) was performed to evaluate the thermal behaviour of the synthesised IONPs in flow. In other words, TGA was used to investigate the temperature related effects of the silica coating on the BIONPs surface as well as the subsequent functionalisation with phenyl groups. The TGA curves of all synthesised IONPs are shown in Figure S13, and the total weight loss percentages are summarised in Table 3. The BIONPs had a total weight loss of around 6.32% (Table 3, entry 1), over the full temperature range (RT to

990 °C), which was comparable to literature.[21] The weight loss below approximately 300 °C, could be attributed to physically adsorbed water to the BIONP surface.[22] Further weight loss from approximately 420°C to 700 °C, could be due oxidation from magnetite to hematite on the nanoparticle surface.[16] The SIONPs had a total weight loss of approximately 8.56% (Table 3, entry 2), which were comparable to reported values.[17,22] This increase in total weight loss compared to that of the BIONPs (Table 3, entry 1) is indicative of successful coating of silica onto the IONPs surface. This weight loss may be attributed to the loss of adsorbed water, propanol, and the decomposition of the silica layer.[23] Upon functionalisation with phenyl groups, the total weight loss increased with an increase in TEPS in TEOS content (Table 3, entries 3-7). Hence, indicating a higher degree of functionalisation (i.e., hydrocarbon character) with an increasing amount of TEPS in TEOS, which resulted in a higher weight loss percentage. These weight losses were attributed to the loss of adsorbed water, propanol, phenyl groups, and the silica layers.

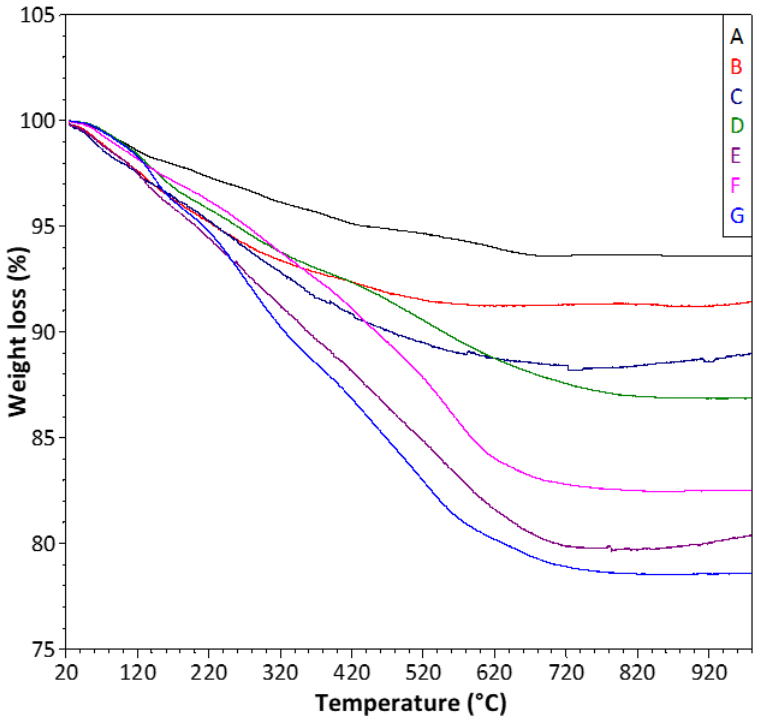

Figure S13: TGA curves of (A) BIONPs, (B) SIONPs, (C) PSIONPs (5.0%), (D) PSIONPs (11.0%), (E) PSIONPs (33.5%), (F) PSIONPs (44.5%), and (G) PSIONPs (50.0%).

References

1 F. Ahangaran, A. Hassanzadeh and S. Nouri, *Int. Nano. Lett.*, 2013, **3**, 23.

2 I. Al Kawni, R. Garcia, S. Youssef, M. Abboud, J. Podlecki and R. Habchi, *Mater. Res. Express*, 2016, **3**, 125024.

3 S. J. Iyengar, M. Joy, C. K. Ghosh, S. Dey, R. K. Kotnala and S. Ghosh, *RSC Adv.*, 2014, **4**, 64919–64929.

4 Z. Bednarikova, M. Kubovcikova, I. Antal, A. Antosova, M. Gancar, J. Kovac, R. Sobotova, V. Girman, D. Fedunova, M. Koneracka, Z. Gazova and V. Zavisova, *Surf. Interfaces*, 2023, **39**, 102942.

5 A. Mokkarat, S. Kruanetr and U. Sakee, *J. Saudi Chem. Soc.*, 2022, **26**, 101506.

6 O. Rezvani, M. H. Hedeshi and H. Bagheri, *Anal. Chim. Acta.*, 2020, **1136**, 51–61.

7 S. Taira, Y. Sahashi, S. Shimma, T. Hiroki and Y. Ichiyanagi, *Anal. Chem.*, 2011, **83**, 1370–1374.

8 S. Taira, D. Kaneko, K. Onuma, A. Miyazato, T. Hiroki, Y. Kawamura-Konishi and Y. Ichiyanagi, *Int. J. Inorg. Chem.*, 2012, **2012**, 1–7.

9 A. M. Faraj Benrabha and K. S. Tay, *Green Process. Synth.*, 2019, **8**, 54–61.

10 F. Vereda, A. Martín-Molina, R. Hidalgo-Alvarez and M. Quesada-Pérez, *Phys. Chem. Chem. Phys.*, 2015, **17**, 17069–17078.

11 S. P. Schwaminger, D. Bauer, P. Fraga-García, F. E. Wagner and S. Berensmeier, *CrystEngComm*, 2017, **19**, 246–255.

12 S. A. A. Noma, A. Ulu, S. Koytepe and B. Ateş, *Biocatal. Biotransform.*, 2020, **38**, 392–404.

13 P. Pinheiro, A. Daniel-da-Silva, D. Tavares, M. Calatayud, G. Goya and T. Trindade, *Materials*, 2013, **6**, 3213–3225.

14 K. Hu, J. Qiao, X. Wu, H. Yang, Y. Huang and S. Zhang, *Microchem. J.*, 2018, **143**, 39–46.

15 J. Zou, Y. Peng and Y.-Y. Tang, *RSC Adv.*, 2014, **4**, 9693.

16 A. H. Gemeay, B. E. Keshta, R. G. El-Sharkawy and A. B. Zaki, *Environ. Sci. Pollut. Res.*, 2020, **27**, 32341–32358.

17 K. Hasan, I. A. Shehadi, K. Ahmed Bagudu, N. Osama Mohamed Elmabrouk, A. Elgamouz, S. P. Patole and R. A. Al-Qawasmeh, *Appl. Surf. Sci.*, 2022, **571**, 151369.

18 F. Chen, Y. Xiao, B. Zhang, R. Chang, D. Luo, L. Yang, Y. Yang and D. Liu, *J. Chromatogr. A*, 2020, **1613**, 460671.

19 M. Saraji and N. Khaje, *J. Sep. Sci.*, 2013, **36**, 1090–1096.

20 M. H. R. Farimani, N. Shahtahmasebi, M. Rezaee Roknabadi, N. Ghows and A. Kazemi, *Phys. E Low Dimens. Syst. Nanostruct.*, 2013, **53**, 207–216.

21 S. Sitthichai, C. Pilapong, T. Thongtem and S. Thongtem, *Appl. Surf. Sci.*, 2015, **356**, 972–977.

22 J. Azadmanjiri, G. P. Simon, K. Suzuki, C. Selomulya and J. D. Cashion, *J. Mater. Chem.*, 2012, **22**, 617–625.

23 C. Turrina, A. Oppelt, M. Mitzkus, S. Berensmeier and S. P. Schwaminger, *MRS Commun.*, 2022, **12**, 632–639.